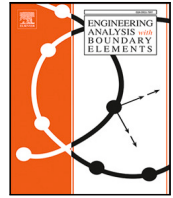




Contents lists available at ScienceDirect

Engineering Analysis with Boundary Elements

journal homepage: www.elsevier.com/locate/enganabound

A hybrid radial basis function-finite difference method for modelling two-dimensional thermo-elasto-plasticity, Part 2: Application to cooling of hot-rolled steel bars on a cooling bed

Gašper Vuga^a, Boštjan Mavrič^{b,a}, Umut Hanoglu^{b,a}, Božidar Šarler^{a,b,*}^a Faculty of Mechanical Engineering, University of Ljubljana, Aškerčeva cesta 6, Ljubljana, SI-1000, Slovenia^b Institute of Metals and Technology, Lepi pot 11, Ljubljana, SI-1000, Slovenia

ARTICLE INFO

Keywords:

Steel bars
Cooling bed
Thermo-mechanical modelling
Hybrid radial basis function generated finite differences
Residual stresses

ABSTRACT

This paper represents Part 2 of the parallel paper Part 1, where the strong form hybrid RBF-FD method was developed for solving thermo-elasto-plastic problems. It addresses the industrial application of this novel meshless method to steel bars cooling on a cooling bed (CB) where the formation of residual stress is of primary interest. The study investigates the impact of the distance between the bars and the distance to the heat shield above the CB on radiative heat fluxes and, consequently, on thermo-mechanical response. The thermal model is solved on bars cross-section with a RBF-FD method where augmented polyharmonic splines are used for the local approximation. View factors, computed with a Monte-Carlo method, are included in radiative heat fluxes. The thermal solution is incrementally applied on a mechanical model that assumes a generalised plane strain state and captures bars bending. The study employs a hybrid RBF-FD method to resolve a nonlinear discontinuous mechanical problem successfully. The simulation of the process shows how different process parameters influence the thermo-mechanical response of the bars.

1. Introduction

After the hot-rolling process, the produced steel bars are placed on the cooling bed (CB), where they are cooled to the desired temperature before being sent to the straightening process. Due to the recrystallisation that occurs because of the combination of high temperatures, strains and strain rates, it is commonly assumed that the bars are free from stress when they exit the final rolling strand. The first stage where residual stresses start to appear is CB. The positioning and geometry of the bar cross-section affect cooling rates, which govern the thermal stresses. Those can exceed yield stress resulting in the accumulation of plastic deformation that leads to residual stresses and bending. The residual stresses can later have an impact on the mechanical response. They can lead to faster initialisation and growth of cracks and shorter fatigue life [1,2]. Large bending of the bars can cause problems during the subsequent straightening process. To efficiently minimise these problems and potentially propose improvements, the computational modelling of the process is crucial.

Previous attempts to model cooling on the CB were mainly focused on rail profiles with symmetric or asymmetric cross-sections. In [3], a 1D thermally loaded thermo-elastic beam resting on a flat rigid

surface was studied. The first thermo-elastic finite element method (FEM) implementation was done in [4], where a beam cross-section was modelled in a generalised plane strain assumption. Later, the model was upgraded with the thermo-elasto-viscoplastic model, which assumed the circular curvature of the beam [5]. In [6], the effect of self-weight was added to describe bending better, and in [7], the same model was successfully verified with experiments. A 3D model was implemented in [8], where the convective heat flux was determined using the Nusselt number correlation. For radiative heat flux, view factors were defined for grey surfaces with no reflection involved. It was found that permanent deformation and residual stresses develop in the early cooling stages when a material is more prone to plastic deformation. In [9], different cooling strategies with water sprays were tested in 3D with the FEM package [10], where friction with CB was considered. The effect of the orientation of the asymmetric rail profile on the CB was investigated in [11]. A 3D model also involving fluid flow simulations was used to determine the convective cooling.

In the present work, the cooling of bars is governed by a heat diffusion equation with temperature-dependent material parameters. The observed problem is modelled in 2D over the bars cross-sections.

* Corresponding author at: Faculty of Mechanical Engineering, University of Ljubljana, Aškerčeva cesta 6, Ljubljana, SI-1000, Slovenia.

E-mail addresses: gasper.vuga@fs.uni-lj.si (G. Vuga), bostjan.mavric@fs.uni-lj.si (B. Mavrič), umut.hanoglu@fs.uni-lj.si (U. Hanoglu), bozidar.sarler@fs.uni-lj.si (B. Šarler).

<https://doi.org/10.1016/j.enganabound.2023.12.001>

Received 31 August 2023; Received in revised form 3 November 2023; Accepted 1 December 2023

Available online 14 December 2023

0955-7997/© 2023 The Author(s). Published by Elsevier Ltd. This is an open access article under the CC BY license (<http://creativecommons.org/licenses/by/4.0/>).

In the calculation of radiative heat fluxes, where a heat shield hanging above the CB is also taken into account, view factors are used to consider the system's geometry. Temperature solution is applied in the mechanical model as the only load. Elasto-plastic material response is considered, and a generalised plane strain (GPS) is employed where the longitudinal strains are linear over the cross-section, and bars are free to bend. No special contact with the CB is considered. The main focus here is to study the effect of the bars and a heat shield positioning on the thermo-mechanical response.

The numerical solution of the problem is performed with the meshless numerical method, described in Part 1 of this paper, which is being published in parallel. In Part 1, this method is derived, implemented, and successfully verified on a simple benchmark that simulates a similar behaviour as the cooling of bars on the CB. For spatial discretisation, a strong form local meshless method [12–17], the so-called radial basis function generated finite difference (RBF-FD) method, and its hybrid variation with finite difference method for a mechanical model are employed. A detailed description of the method can be found in [18].

The main originality of this paper can be summed as:

- The implementation of view factors into radiative heat fluxes within the RBF-FD method.
- The application of the RBF-FD method to model the thermo-mechanical response of steel bars on the cooling bed.
- The study of the effect of the distance between the bars and positioning of the heat shield.

The present paper is structured in the following order. The considered problem is formulated in Section 2. Next, the simulation procedure of cooling steel bars with the used parameters is given in Section 4, and the results are presented in Section 5. Lastly, the conclusions are provided in Section 6.

2. Formulation of the problem

After the hot-rolling process, a bar is transported to the CB. Since the length of the bar is long compared to the bar cross-section, and the cooling conditions are assumed to be constant along its length, the uniform longitudinal temperature assumption is employed. The domain of interest is thus reduced to the bar cross-section. Here, the flat bars with a cross-section of 80×39 mm are studied.

The cooling process starts when the first bar is transported from the hot-rolling process and occupies position p_1 as shown in Fig. 1(a). After time $t = t_p$, the bar is lifted and moved to the next position p_2 and at the same time, a new bar arrives at position p_1 (Fig. 1(b)). After t_p , these 2 bars are moved by one position, and a new bar comes to p_1 (Fig. 1(c)). This movement is repeated until bars reach the last position p_n (Fig. 1(d)), where they are in the next step removed from the cooling bed and transferred further to a straightening process (Fig. 1(e)).

The bars are positioned close to each other and thus affect their radiative cooling rate. As shown in Fig. 2, a heat shield of length p_l is also placed above the CB at the distance of p_y , which impacts the radiation. Below the bars, the construction for holding them, which is schematically shown with the “saw” curve, consists of longitudinally equally spaced thin supports. Since the contact with the supports is small compared to the whole bar length, we assume they do not affect cooling.

The main aim of this work is to study the effect of the heat shield position p_y and the distance between bars x_{bp} , which corresponds to the number of empty positions, on the thermo-mechanical response during the cooling process.

3. Model description

Thermal and mechanical models are explained in detail in Part 1. of this paper. In this section, a few additions specific to the problem are described.

3.1. Thermal model

Cooling of the steel bars is governed by the heat diffusion equation

$$\frac{\partial \rho c_p T}{\partial t} = \nabla k \cdot \nabla T + k \nabla^2 T, \quad (1)$$

that is solved for temperature T . ρ , c_p , and k stands for density, specific heat at constant pressure, and thermal conductivity, respectively, that are temperature dependent. On the boundary, the heat flux in the normal direction \mathbf{n} is prescribed as

$$q_n = \mathbf{q} \cdot \mathbf{n} = -k \frac{\partial T}{\partial n} = q_{conv} + q_{rad}, \quad (2)$$

where the heat flux is defined by the Fourier's law $\mathbf{q} = -k \nabla T$. The convective heat flux q_{conv} is specified by

$$q_{conv} = h_f (T - T_{amb}), \quad (3)$$

where h_f and T_{amb} stand for the heat transfer coefficient and ambient temperature, respectively. Since it is known that convection has a minor effect compared to radiation at high temperatures, no special treatment of h_f is carried out as it was done in [8] with empirical modelling or in [11] with complete fluid flow analysis. A constant value is used on all boundaries. Regarding radiation, the observed objects (steel bars and heat shield) at high temperatures significantly affect each other. Due to that, the geometry and positioning of the objects are additionally incorporated into the definition of radiative heat flux q_{rad} , also prescribed on the boundary. As shown in Fig. 3, the boundary of steel bars (red line) and heat shield (blue line), is discretised on finite length sections (FLSs). The FLSs are separated by black dots and enclosed with a discretised closed-loop virtual boundary (green line) representing all the surroundings. The net radiative heat flux of the i th FLS $q_{rad,i}$ is given as a difference between the emitted heat flux from the i th surface and received heat flux from all surrounding FLSs written in the form of

$$q_{rad,i} = \epsilon_i \sigma T_i^4 - \sum_{j=1}^J \epsilon_j \sigma T_j^4 \frac{L_j}{L_i} F_{j \rightarrow i}, \quad (4)$$

where the sum goes over all (J) FLSs, where L_j represents the length of a j th FLS. The emissivity is denoted with ϵ and the Stefan–Boltzmann constant with σ . The visibility between FLSs is given by a view factor $F_{j \rightarrow i} \in [0, 1]$. It defines the fraction of the radiation emitted by the j th FLS and received by i th FLS [19].

For each pair (j, i) of FLSs (shown in Fig. 3), a view factor $F_{j \rightarrow i}$ has to be defined. Values are compactly denoted with a view factor matrix F that includes all view factors of the observed system. In this work, F is computed using the Monte Carlo method [20]. From each j th FLS, N_{vf} particles are shoot in a random direction and checked which i th FLS is hit. Based on the number of particles that hit i th FLS, the $F_{j \rightarrow i}$ value is determined. As previously shown in [21], the number of particles is chosen to be $N_{vf} = 10^6$ in order to keep the uncertainty of computation below 1%. To include also the effect of reflectivity $\zeta \in [0, 1]$, $N_{vf} \cdot \zeta$ random particles are bounced off the FLSs that have $\zeta > 0$. A more detailed description of the related algorithm can be found in [22].

Since the Monte Carlo procedure is computationally very involved, the number of FLSs significantly affects the computational time for determining F . To reduce the computational time and still reasonably well describe the effect of geometry and positioning on the cooling, the FLSs on the bars are not prescribed for each boundary discretisation node (DN). An algorithm that groups boundary DNs, based on the normal vectors change and maximum distance, is employed that results in the sectioning presented in Fig. 3. Here a total of 25 FLSs are generated per bar. The effectiveness of FLS discretisation is presented in Section 5.1. Since the heat shield is assumed to be at a constant temperature, only one FLS is assigned to it. Based on the temperature solution in DNs belonging to i th FLS, a constant averaged heat flux is applied in all DNs on the i th FLS. Averaging of the heat flux, given by Eq. (4), is done by averaging only the temperature term as $T_k^4 = 1/N_k \sum_{l=1}^{N_k} T_l^4$ where k is i or j if FLS lies on the bar. The sum runs over N_k boundary nodes that belong to the k th FLS.

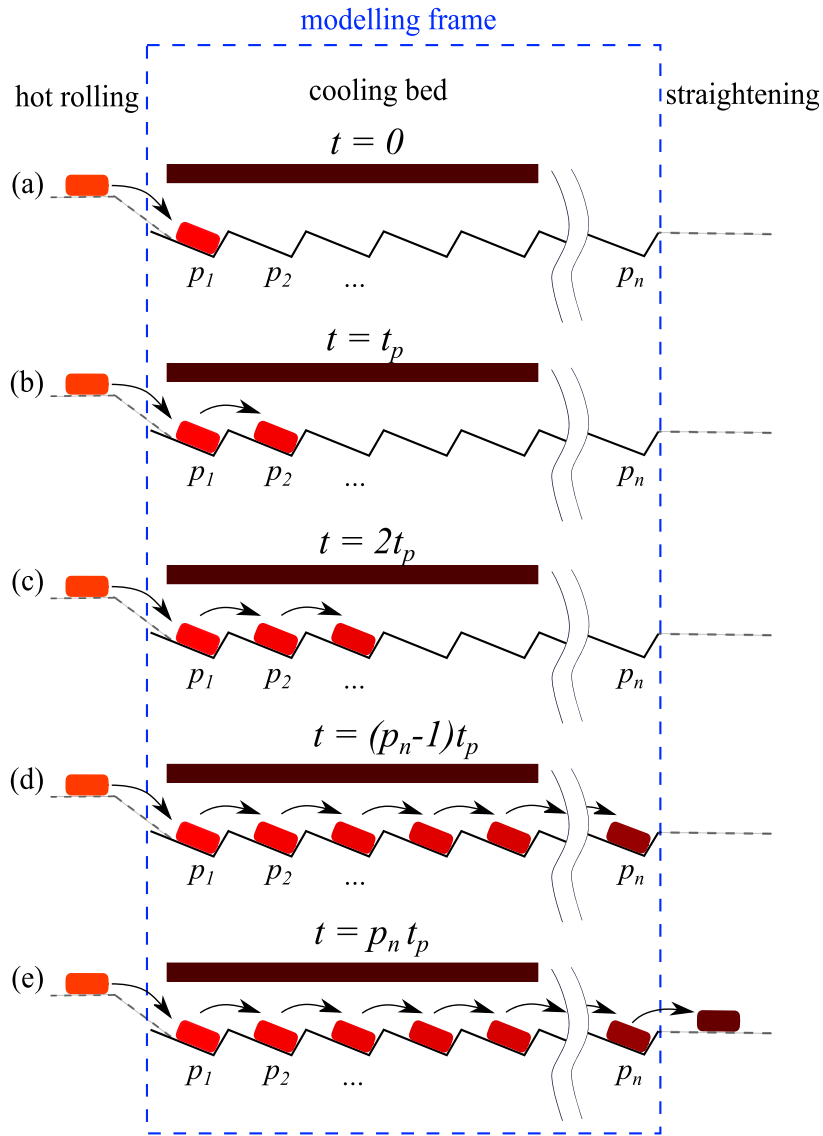


Fig. 1. Transport of bars on the cooling bed in a cross-section.

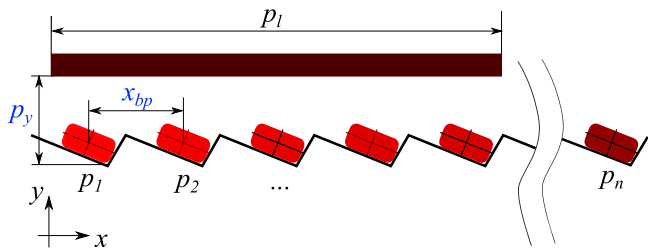


Fig. 2. Cross-section scheme with labelled dimensions.

3.2. Mechanical model

Steel has a low strength at high temperatures, and yielding can occur at small loads. So the mechanical response is assumed to be elasto-plastic where small-strain von Mises isotropic plasticity is considered. In this work, a Jonson–Cook strain rate independent hardening law is employed as

$$\sigma_y(T, \bar{\epsilon}^p) = (A + B(\bar{\epsilon}^p)^n) \left(1 - \left(\frac{T - T_0}{T_m - T_0} \right)^m \right), \tag{5}$$

where constants A, B, T_0, T_m, n, m are determined by fitting the experimental data. Material parameters used; Young’s modulus E , Poisson ratio ν , and linear expansion coefficient α are treated as temperature dependent.

In terms of boundary conditions (BCs), no special contact with CB supports is considered. On the whole boundary, traction BCs with zero load are imposed. In order to obtain a unique solution, two additional regularisation constraints are defined

$$\int_{\Omega} \mathbf{u}(\mathbf{r}) d\Omega = 0, \quad \int_{\Omega} (\mathbf{u}(\mathbf{r}) \times \mathbf{r}) d\Omega = 0, \tag{6}$$

that restrict relative translations and rotations. Discretisation of integrals is performed as a sum over all DNs $\sum_{i=1}^N y(\mathbf{r}_i) = 0$, where y refers to translation or rotation.

To capture the bending of bars, the introduced model assumes a generalised plane strain (GPS) approximation. Since no contact is assumed, bars can freely bend and shrink. In additional equations of GPS, the prescribed values of longitudinal force and two momentums are set to zero $\{\hat{N}_z, \hat{M}_x, \hat{M}_y\} = \{0, 0, 0\}$ and solved for constants $\{a, b, c\}$ that are used in a linear definition of the longitudinal strain $\epsilon_{zz} = ax + by + c$.

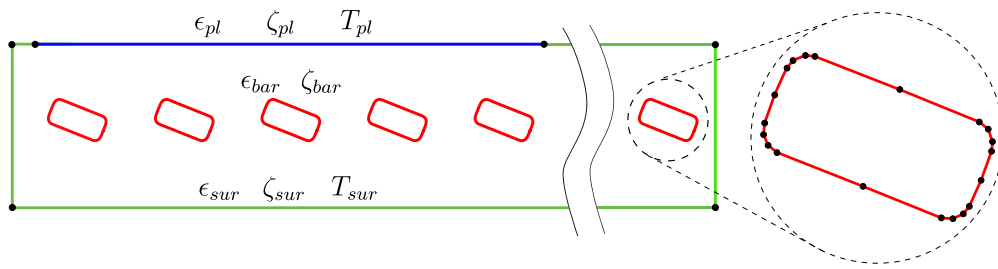


Fig. 3. Scheme of boundaries used for radiative heat flux determination.

4. Solution procedure for modelling the cooling of steel bars

The simulation is performed as a one-way coupled as the benchmark study presented in Part 1 of this paper. The thermal problem is solved first. Spatial discretisation is performed with the RBF-FD, where geometry is discretised with a homogeneous distribution of discretisation nodes. Differential operators are evaluated in a finite difference-like manner, where operator weight coefficients must be locally computed for each local support stencil. As in Part 1, the third-order polyharmonic splines with the second order augmentation are employed to construct interpolants. Thirteen nodes are included within local supports to obtain the h-convergence governed by the augmentation order, as shown in Part 1. Time marching is performed with the explicit Euler scheme, where the time step is defined as $\Delta t = \alpha_{\Delta t} \frac{h^2 \rho c_p}{4k}$. h represents the minimum distance between DNs and $\alpha_{\Delta t}$ is the time stability parameter for which it was found in Part 1, that it must be $\alpha_{\Delta t} = 0.5$ or less for the method to be stable. Here $\alpha_{\Delta t} = 0.5$ is used.

In Fig. 4, the procedure for solving the thermal problem is shown schematically. At first, the resulting discretised geometry of the bar, coming from the hot-rolling simulation system [23,24], is imported. As shown in Fig. 5, the discretised geometry is extended from one quarter to the whole section with 5881 discretisation nodes. Then, the bar's boundary is discretised on FLSs and positioned on the first position p_1 inside the closed loop, as shown in Fig. 3. With one bar on the cooling bed, the view factor matrix F is computed as described in Section 3.1. The initial temperature of the bar $T_{bar,0}$ (at $t = 0$ on p_1) is assumed to be constant over the cross-section.

Temperatures of the heat shield T_{pl} and the surroundings T_{sur} are constant over time. They are used only to determine the radiative heat fluxes. With temperatures and view factor matrix, the heat fluxes \hat{q} are computed, where parameters presented in Table 1 are used. Diffusion in the bar is then solved until time t_p is reached, where during time marching, the heat fluxes \hat{q} are updated based on the temperature solution. After that, the bar is moved to p_2 , and a new bar is positioned on p_1 . With 2 bars in the system, a new F is computed. Initial temperatures are now $T(r, t_0, p_1) = T_{bar,0}$ and $T(r, t_0, p_2) = T(r, t_p, p_1)$, where the transport time between positions is neglected. From here, again, \hat{q} is determined, and the simulation runs until t_p , now with 2 bars cooling. Then, 2 bars are moved forward, a new one comes in, and the process repeats. This process continues until the temperature profile of the bar that entered the cooling bench first is computed at the final position p_n . Then, a bar on p_n is removed from the system, the rest is moved forward, and a new one comes to p_1 . Then, the simulation runs again, and the process repeats until the temperature difference ΔT between two cycles, in the centre of the bar on p_n , is less than ΔT_{max} . This simulation procedure results in a quasi-steady state solution.

The resulting temperature solution is position (stage) dependent $T(r, t_j, p_i), t_j \in [0, t_p], i = 1, \dots, n$. For use in the mechanical simulation on one bar only, it is transformed to $T(r, t_j), t_j \in [0, t_p n]$. This temperature history is then incrementally applied as external thermal load in the mechanical simulation. To successfully resolve the nonlinear mechanical problem, a denser node arrangement with 13152 nodes is employed where the temperature is interpolated. The mechanical

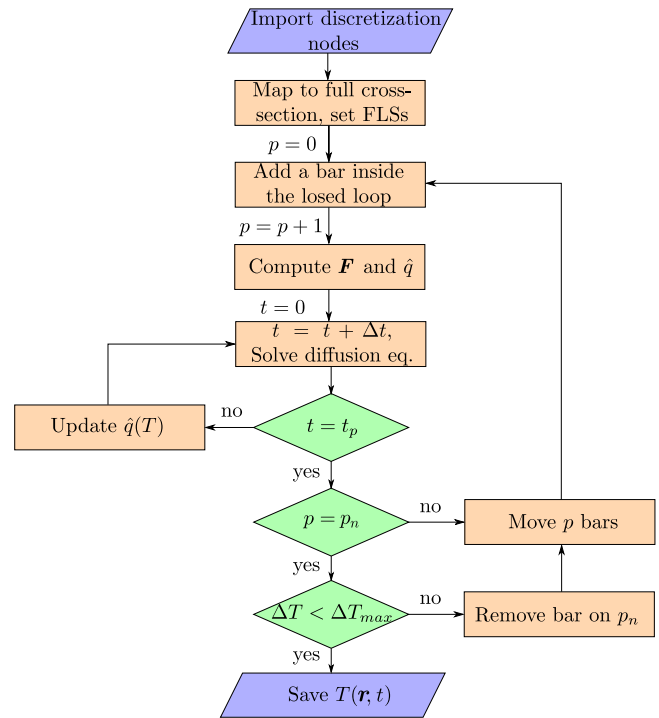


Fig. 4. Simulation procedure of thermal problem.

model is spatially discretised with the Hybrid RBF-FD [18], as described in Part 1. The finite difference stencil size is set as $\alpha_D h = 0.5 h$, and BCs are evaluated for $\alpha_S h = 0.1 h$ away from the boundary in the opposite direction of the outward-facing normals. The maximum residual in the Newton–Raphson iteration process is set to 10^{-7} .

The material parameters used are temperature dependent and are updated after each time step in the thermal simulation and after each load increment in the mechanical simulation. In this work, the material parameters for a 46MnVS5 steel are used. Those are $k(T), c_p(T), \rho(T), E(T), \nu(T)$, and $\alpha(T)$. For the chosen material, they were prepared with the JMatPro software [25].

As mentioned, the effect of the distance between the cooling bed and the heat shield p_y and the distance between bars x_{bp} on the thermo-mechanical response is studied. The study is performed for three (R1, R2, R3) different cases of the distance between bars where values of x_{bp} are given in Table 2. To study the same time window, where $t_{max} = t_p n$, different times per stage t_p , and different maximum number of stages n is applied. Along with three x_{bp} 's, another three (P1, P2, P3) distances of the heat shield p_y is studied, resulting in nine different cases.

The simulation procedure was executed using the same programming language and performed on the same hardware platform as in Part 1.

Table 1
Constants used in the thermal model.

$\epsilon_{pl}, \epsilon_{bar}, \epsilon_{sur}$ [J]	ζ_{pl}, ζ_{bar} [J]	ζ_{sur} [J]	T_{pl} [°C]	$T_{bar,0}$ [°C]	T_{sur} [°C]	h [W/ m ² K]	ΔT_{max} [°C]
0.8	0.2	0	300	900	20	20	0.5

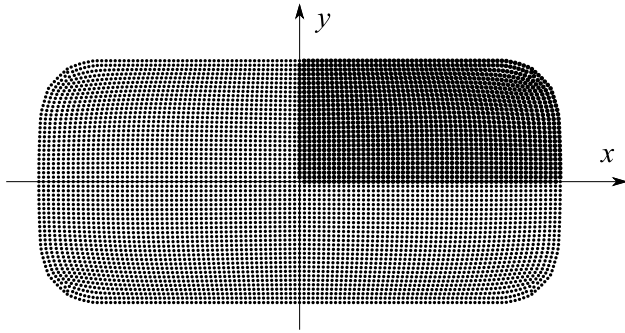


Fig. 5. Rectangle bar cross-section (80 × 39 mm) discretised with 5881 nodes. Thick nodes represent the input values from the hot-rolling simulation system [23,24].

Table 2
Cooling bed process parameters variation.

	x_{bp} [m]	t_p [s]	n [/]	p_y [m]
R1	0.14	5	30	P1
R2	0.28	10	15	P2
R3	0.42	15	10	P3

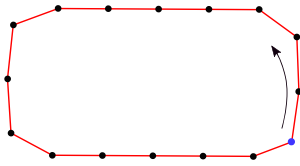


Fig. 6. Example of a bar sectioning on FLSs with $\kappa = 20$.

5. Results of a thermo-mechanical response

5.1. Performance of the view factors computation

In order to observe the computational efficiency and accuracy of determining $F = F_{ij}$, we first look at the simplified case with only 3 bars in the system positioned on p_1, p_2, p_3 (see Fig. 2). We can assume that the middle bar on p_2 experiences typical radiative conditions since most of the bars in the system (assuming reflectivity is negligible) see their neighbours only. For maximum effect, we set a small value in x_{bp} (same as P1 case) and in p_y (same as R1 case). FLSs on bars are prescribed in a consecutive order, as shown in the example in Fig. 6. The blue node is taken to be the first splitting node, and each κ -th boundary DN in the direction of the arrow becomes the subsequent splitting node. In Fig. 6 $\kappa = 20$.

The resulting F of a system with 3 bars and $\kappa = 20$ is shown in Fig. 7. Components within a purple rectangle, denoted as \hat{F}_{ij} correspond to the $F_{j \rightarrow i}$, where j goes over the FLSs of the middle bar.

To show the performance in terms of the N_{vf} , we investigate the relative error e_2 defined as

$$e_2 = \sqrt{\frac{\sum_i |F_{i22} - \tilde{F}_{i22}|^2}{\sum_i |\tilde{F}_{i22}|^2}} \quad (7)$$

where $j = 22$ represents the first FLS on the middle bar (first column in \hat{F}_{ij}). The reference solution \tilde{F}_{i22} is obtained with $N_{vf} = 10^7$. In Fig. 8 the e_2 convergence is presented. It can be seen that the convergence

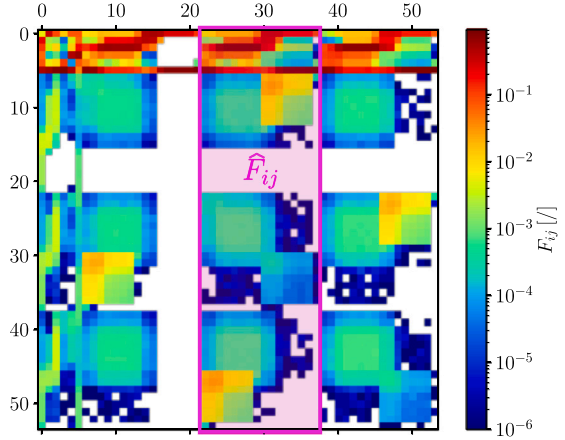


Fig. 7. F_{ij} for 3 bars in a closed system determined with $\kappa = 20$ and $N_{vf} = 10^6$.

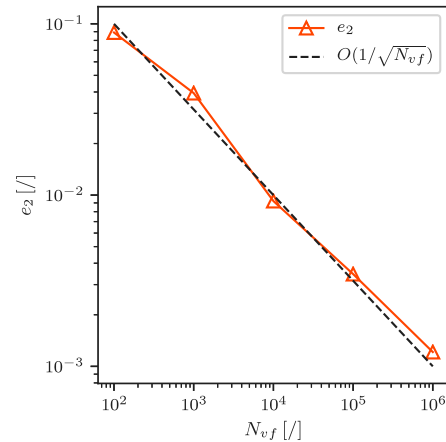


Fig. 8. Convergence of F_{i22} computation with increasing N_{vf} .

rate follows $1/\sqrt{N_{vf}}$, as expected for the Monte-Carlo integration procedure [20].

To show that the FLSs that lay on the same straight line can be grouped, the properties of the matrix $G = \hat{F}^T \cdot \hat{F}$ that show how similar are the columns of \hat{F} to each other. Here \hat{F} represents \hat{F} centred in the centroid as $\tilde{F}_{ij} = \hat{F}_{ij} - c_i$ with $c_i = \sum_j \hat{F}_{ij} / i_{max}$. In Fig. 9, resulting matrices of G for different κ s are presented. Observing G with $\kappa = 3$ along the diagonal direction, one can identify four blocks, each having similar values of G . The two smaller blocks correspond to the short sides of the bar, while the two larger blocks correspond to the long sides. Same value in G within blocks represents a similar direction of vectors (columns) of \hat{F} . Moving to larger κ s it can be seen that these blocks stay present in a similar structure. This shows that grouping of FLSs, laying on the same straight lines, can be done without much of an impact on F .

To further explore the effect of grouping FLSs, temperature solutions over field $T(r, t)$, obtained with $\kappa = 3$ (105 FLSs) and optimised discretisation presented in Fig. 3 (25 FLSs), are compared. Results are computed with 3 bars in the system where these are first sequentially added and moved and then left stationary without further movement for a total of $t_{max} = 150$ s. In Fig. 10(a), $T(r, t = 150$ s) is shown, obtained on the optimised discretisation. It can be seen that the solution

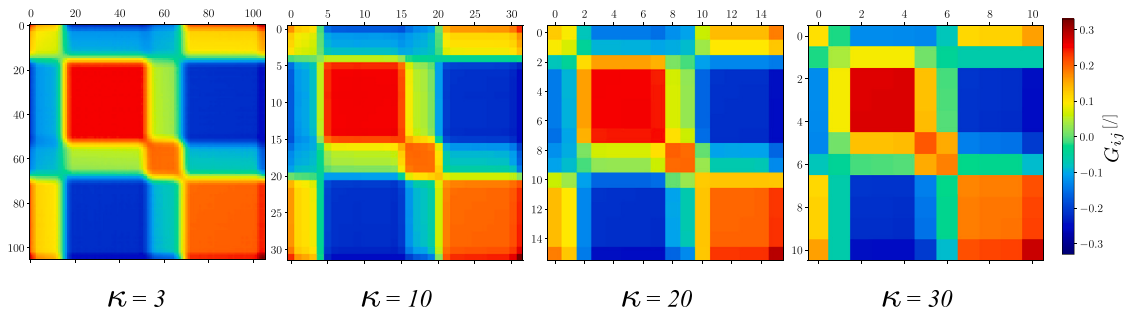


Fig. 9. Matrix G_{ij} for different values of κ .

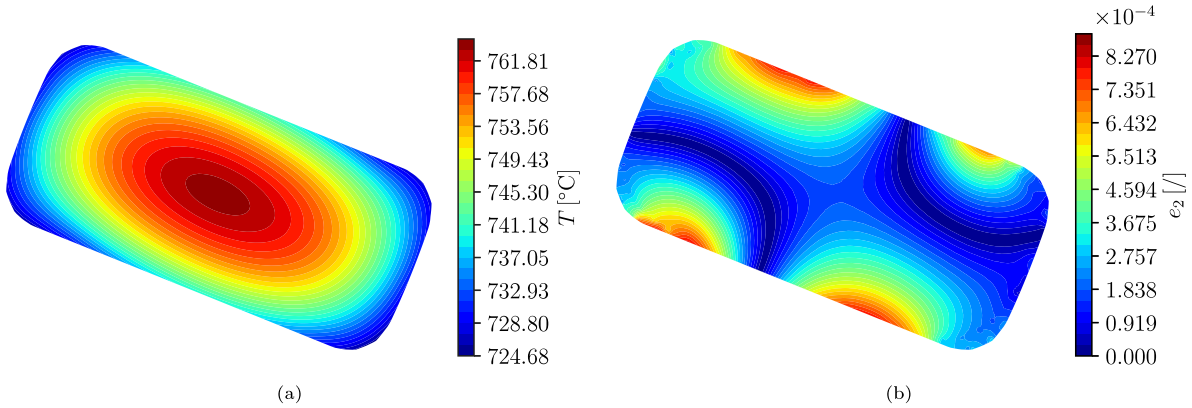


Fig. 10. $T(r, t = 150 \text{ s})$ solution obtained with optimised discretisation on FLSs (a), error between solutions obtained with optimised discretisation and with fixed lengths where $\kappa = 3$ (b).

is smooth and slightly tilted due to the radiative effect. In Fig. 10(b), the error over field, defined as $e_{2,i} = |T_i - \hat{T}_i|/|\hat{T}_i|$, where $i \in \{1, N\}$, and \hat{T} is obtained with $\kappa = 3$, is shown. It can be seen that the largest values are at the long sides of the bar where the discretisation is coarse, but overall, the $e_{2,i}$ is relatively small, within a range of $\sim 10^{-4}$. This suggests that the optimised grouping of FLSs does not significantly compromise the overall accuracy of the thermal model.

5.2. Thermal response

In Fig. 11, the minimum value of temperature in the bar for the P1R1 case (T_{P1R1}) and the differences to other cases $T_{diff} = T_{P1R1} - T_{P1Ri}$ are plotted over time. Due to the heat shield being positioned at its lowest point and the bars being closely spaced in the P1R1 case, the cooling rate is the lowest. A significant temperature drop is observed initially because of the constant temperature T_0 at time zero. The temperature profile eventually becomes linear and drops a bit more at the end when the bar reaches the final position p_n . Cooling is here more significant because the bar is not positioned between 2 bars but has only one neighbour, like on p_1 . Comparing results with P2R1 and P3R1, a slight difference can be seen ($< 1 \text{ }^\circ\text{C}$) that slowly increases up to t_{out} and then stays constant for P2R1 and reduces a bit for P3R1. The time t_{out} indicates when the bars are no longer located beneath the heat shield.

The difference between R1, R2 and R3 is up to $t_p(R1)$ negligible. As the bar in R1 advances on p_2 , its cooling rate slows down due to the presence of the left and right neighbouring bars, while in R2 and R3, bars remain in p_1 and continue to cool at a faster rate, causing the difference to increase. Once the bars in R2 and R3 also reach p_2 , the difference decreases because the cooling rate decreases due to the left and right neighbours. From here on, the difference increases and has a steeper slope in R3 where the spacing x_{bp} is larger, meaning the bars have less effect on each other regarding radiative heat flux. After

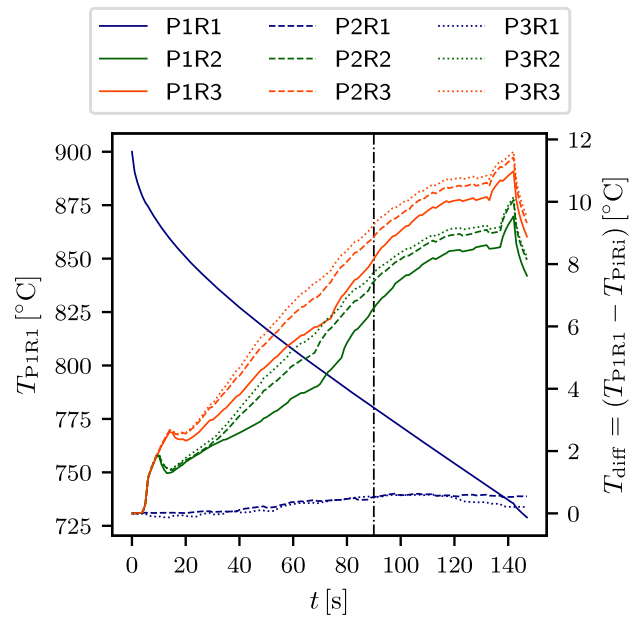


Fig. 11. The minimum temperature inside the bar for the P1R1 case and the difference with other cases over time.

t_{out} , the slope of the difference starts to decrease. When bars in R2 and R3 reach p_n , the difference increases because the bars have only a left neighbour, and the bar in R1 at that time did not yet reach p_n . When R1 reaches p_n , the difference decreases since R1 also starts to cool faster. The results between P1, P2 and P3 are not changing much. The cooling rate is highest in P3, where the distance to the heat shield is the largest.

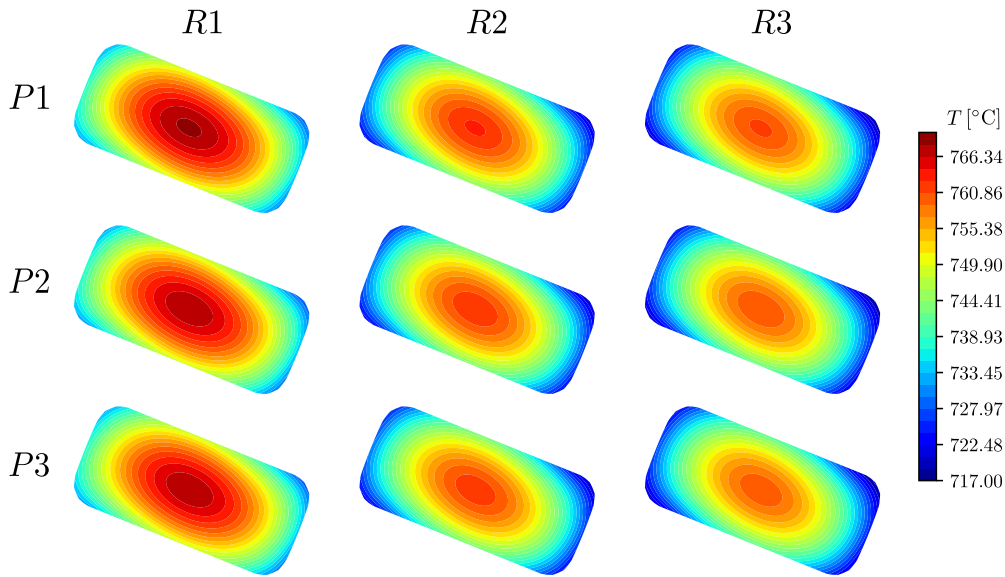


Fig. 12. Temperature solution over the field at t_{max} for all cases.

Effectively comparing results, the maximum difference between $P1R1$ and $P1R2$ is $\sim 9^\circ\text{C}$ within the observed time frame. Increasing space from x_{bp} ($R2$) to x_{bp} ($R3$) changes the results for only $\sim 2^\circ\text{C}$. Also, changing the heat shield position changes the result for a maximum $\sim 2^\circ\text{C}$.

Fig. 12 shows the temperature solution over the field at $t = t_{max}$ for all cases. It can be seen that the temperature is not symmetric due to non-uniform heat flux. In all cases, the right side is colder than the left side of the bar. This occurs since the right neighbouring bars are colder, so a larger heat flux is present on the right side. As previously shown, the impact of increasing the space between bars x_{bp} (see from left to right) is more significant than increasing the distance to the heat shield p_y (see from top to bottom).

To investigate the asymmetry of the solution in detail, we introduce a measure of the averaged difference over the x and y axes

$$\bar{T}_x = \frac{1}{n_{xp}} \sum_{i=1}^{n_{xp}} (T_i - T_{x(i)}), \quad \bar{T}_y = \frac{1}{n_{yp}} \sum_{i=1}^{n_{yp}} (T_i - T_{y(i)}), \quad (8)$$

where i runs over n_{xp} or n_{yp} nodes for which $x > 0$ or $y > 0$ (assuming the geometry is centred at $(0, 0)$ as shown in Fig. 5). Mapping $\mathcal{X}(i)$ provides an index of the node with a negative x value; similarly, $\mathcal{Y}(i)$ provides an index of the node with a negative y value.

In Fig. 13, averaged differences over the axes are shown in time. Observing \bar{T}_x , one can see that the curve is positive in the beginning since greater heat flux is present on the boundary with $x < 0$ and on average right side $x > 0$ is hotter. After t_p , when the bar is moved on p_2 , values become negative since greater heat flux is present on $x > 0$ side, and the right side is colder. After t_{out} , when bars are not under the heat shield any more, the heat flux increases, especially on the top and the left side of the bars. This affects most of the P_1 cases. It can be seen (especially for $P1$) that \bar{T}_x starts to increase after t_{out} . When bars reach the last position p_n , the greater heat flux from the right side has a dominant effect. This results in an even colder right side. In terms of \bar{T}_y , the effect of the heat shield is seen up to t_{out} . The top side is hotter than the bottom side in all cases. After t_{out} , asymmetry in y starts to decrease and even goes to the negative side at the last stage p_n , since the top half becomes cooler due to the absence of the right neighbour. Effectively, averaged differences do not change for more than $\sim 2.5^\circ\text{C}$.

5.3. Mechanical response

The displacement field that is consistent with the definition of the longitudinal strain ϵ_{zz} also includes dependency in the z -axis and is

defined as

$$\mathbf{u}(x, y, z) = \begin{pmatrix} u_x(x, y) + u_x(z) \\ u_y(x, y) + u_y(z) \\ u_z(z) \end{pmatrix} = \begin{pmatrix} u_x(x, y) - a z^2/2 \\ u_y(x, y) - b z^2/2 \\ (ax + by + c) z \end{pmatrix}. \quad (9)$$

Using this expression when deriving strain tensor by definition $\epsilon = \frac{1}{2} (\nabla \mathbf{u} + \nabla \mathbf{u}^T)$, linear longitudinal strain $\epsilon_{zz} = ax + by + c$ is also obtained. Assuming a finite length of a bar, $L = 40$ m, the deflection at the ends is expressed as $u_x(z = L/2)$ and $u_y(z = L/2)$. In Fig. 14, deflections in the x (left) and y (right) axes are shown in time.

One can see that the deflection trend is the same as the temperature averaged difference but with the opposite sign since a bar tends to bend in the direction of lower temperature. A comparison between cases shows that the $P1R1$ case, with the most asymmetric cooling, experiences the most changes and reaches extreme values during cooling. On the other hand, the $P3R3$ case, which has the most homogeneous cooling, is prone to smoother transition and reaches the lowest values. Larger maximum deflections are obtained in the y -direction since the 2nd moment of the area around the x -axis is smaller than around the y -axis. The maximum size of deflections is $u_{x,max} \sim 0.130$ m, and $u_{y,max} \sim -0.3$ m. It should be noted that, in reality, contact with the cooling bed and a self-weight of the bar can have a significant impact on the final deflection size.

Figs. 15 and 16 show field values of von Mises stress and accumulated plastic strain at time t_{max} , respectively. Due to the high-temperature gradients at the beginning of the cooling, the outer layer of the bar tends to shrink, but the inside material prevents this from occurring. Consequently, tensile stresses are induced on the boundary and compressive ones inside. Since initial yield stresses are low at high temperatures, the material yields. This happens at first on the boundary, where gradients are high. Later, when compressive stresses inside the bar become high enough and temperatures are still high, plastic strain is induced at the centre and expands in a radial direction. This distribution of accumulated plastic strain can be seen in Fig. 16 at $t = t_{max}$ and is similar to the one presented in the benchmark test in Part 1. In Fig. 17 (right), where maximum values of $\bar{\epsilon}^p$ over time are shown, one can see that no change happens after ~ 20 s. At this point, yielding stops since the yield curve is growing with decreasing temperature at a higher rate as thermal stresses are induced. Maximum values at ~ 10 s are located on the boundary and later at the centre of the bar. Small changes between cases are observed where the maximum difference between $P1R1$ and $P3R3$ equals $\sim 7 \cdot 10^{-5}$.

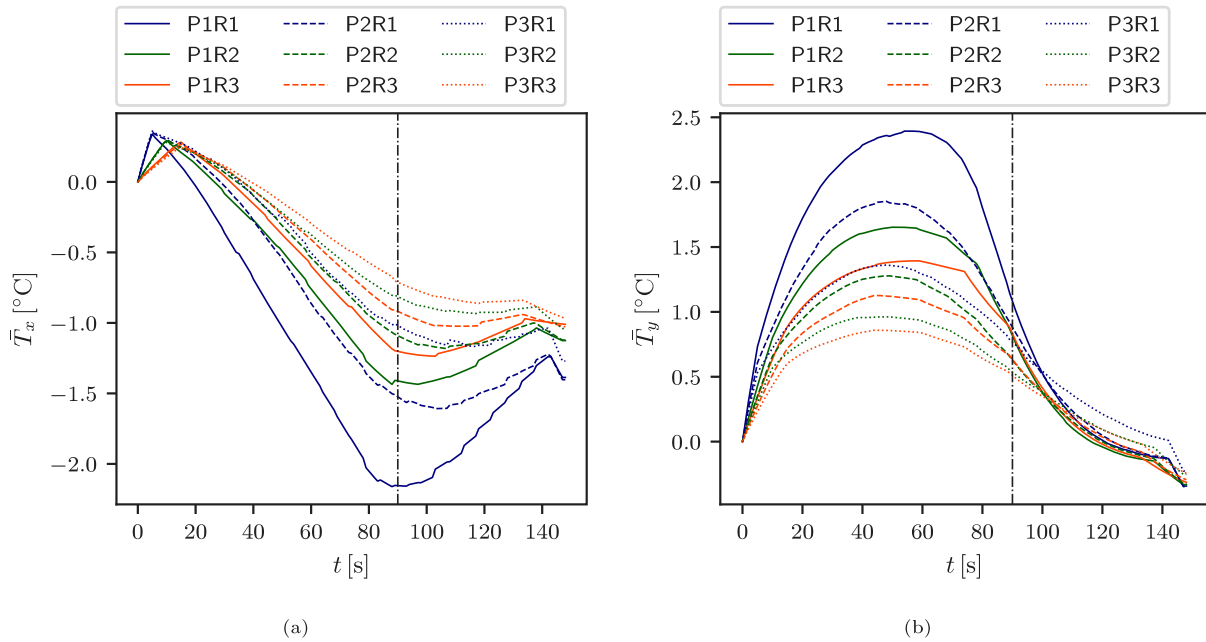


Fig. 13. Temperature averaged differences over the x-axis (a) and the y-axis (b) in time.

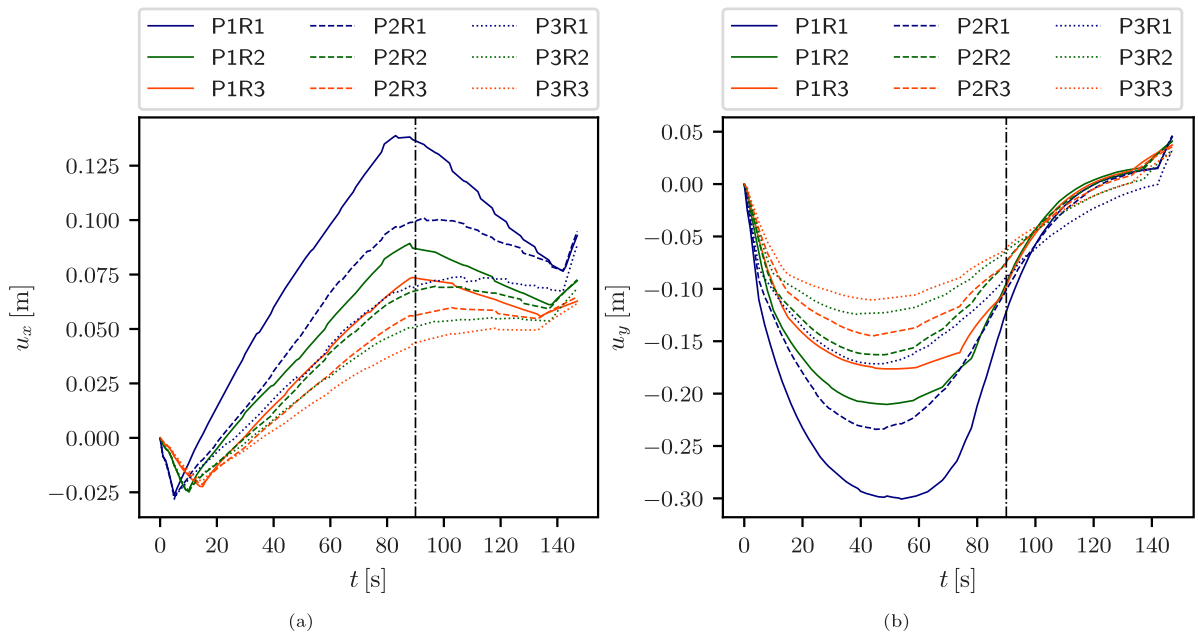


Fig. 14. Deflection in x (a) and y (b) axes over time at the bar ends; $L/2 = 20$ m.

The von Mises stresses, shown in Fig. 15, evolve over the whole time frame and reach maximum values in the upper-right corner where the bar is coldest. The distribution of σ_{vm} has more of a diagonal symmetry due to the final (Fig. 12) and history of temperature distributions. The time dependence of maximum σ_{vm} is shown in Fig. 17 (left), where it can be seen that σ_{vm} is increasing until ~ 35 s for R1 cases and until ~ 45 s for R2 and R3 cases due to the increasing difference in temperature between the boundary and centre. Later, this difference decreases, and the temperature profile slowly flattens, so the stresses also decrease. At the last stage p_n , where increased cooling is present on the right side of the bar, the temperature difference increases and consequently also σ_{vm} . The maximum value of σ_{vm} obtained equals ~ 35 MPa. A similar range solution (~ 25 MPa) was observed in the study of [7] where the cooling of the rectangle was validated with experiment. They also showed that

the difference between a full 3D model and a 2D generalised plane strain approach can be, in terms of effective stress, around 15%. Small changes can be observed when comparing results with different heat shield positioning (P1, P2 and P3). Higher values of σ_{vm} are obtained in cases with bigger spacing between bars since more considerable temperature differences are present over the domain. The maximum difference between R1 and R3 cases equals ~ 5 MPa.

In Fig. 18, the initial and final shape of the bar is shown for P1R1, P2R2, and P3R3 cases. Other cases with different Ps are not present since they are very similar to the one presented. The initial shape is shrunk by a factor of 2 for a clear presentation of the results. Deformed contours are obtained by applying displacement field values, multiplied by 300, onto the initial geometry.

As expected, the deformed bar has a bulged shape contour. Due to the temperature distribution, it is slightly tilted to the left.

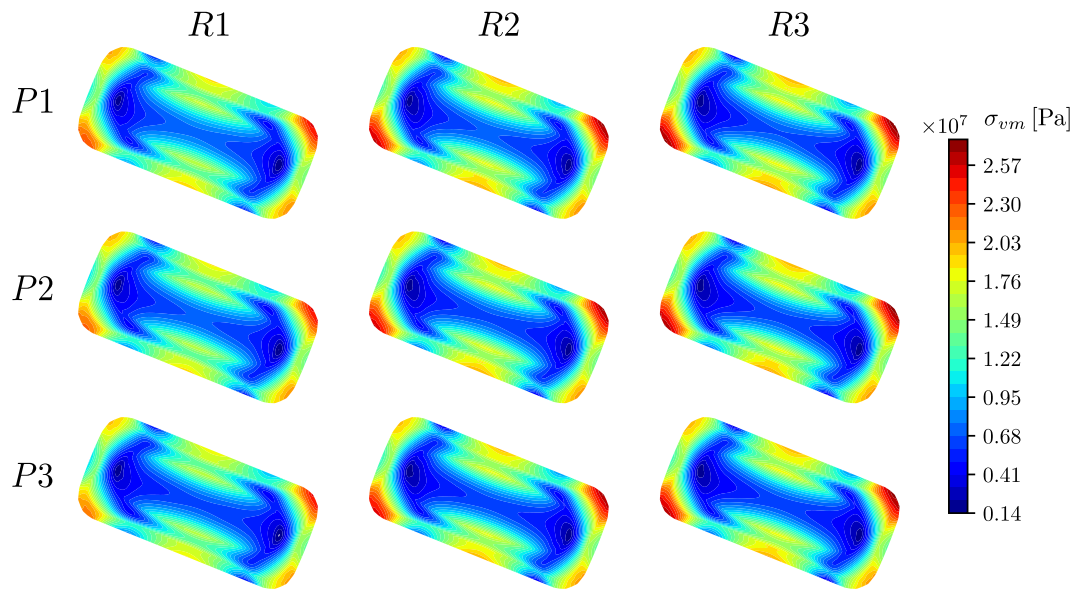


Fig. 15. Von Mises stress solution over the field at t_{max} for all cases.

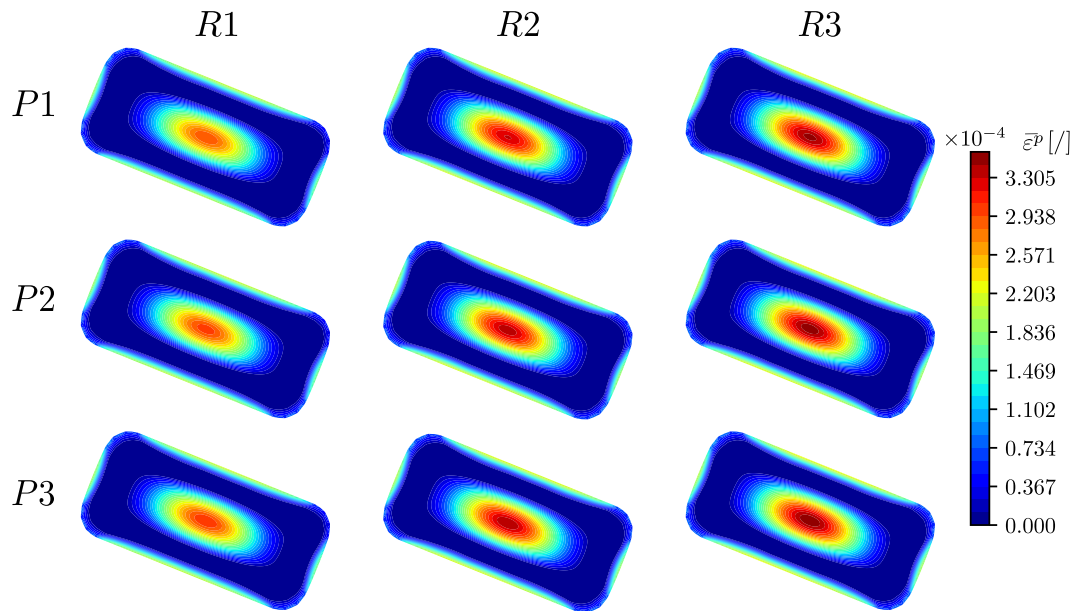


Fig. 16. Accumulated plastic strain solution over the field at t_{max} for all cases.

6. Conclusions

In this work, the capabilities of the RBF-FD method for solving a complex industrially relevant thermo-mechanical process of cooling steel bars on the cooling bed are demonstrated.

The study investigated the heat shield positioning p_y and the distance between bars x_{bp} regarding the impact on the thermo-mechanical response inside bars. For the first time, view factors are included in RBF-FD thermal model for radiative heat fluxes computation. Numerical parameters used to successfully resolve the presented benchmark in Part 1 were employed in the simulation system to model steel bars' cooling.

It was found that x_{bp} has a major effect on the cooling rate, where doubling the x_{bp} resulted in $\sim 9^\circ\text{C}$ difference in the lowest temperature at the end of the observed time frame. Interestingly, tripling x_{bp} , resulted only in an additional $\sim 2^\circ\text{C}$ difference. The same maximum

difference was observed with changing p_y . The temperature distribution was found to be asymmetric over the axes due to non-homogeneous heat fluxes. The most asymmetric case was the one with the smallest x_{bp} and p_y , since surrounding objects are at the closest distance. The average temperature difference above the axes stays below 3°C .

It turns out that the evolution of the averaged temperature difference has exactly the same trend as a bar deflection but with the opposite sign. The maximum deflection obtained on a bar with $L = 40\text{ m}$ is $\sim 0.3\text{ m}$. The resulting stress field follows the temperature distribution, where due to high-temperature gradients at the start, all of the plastic deformations occur in the initial cooling stages. Again, a small impact of p_y is observed on solution fields. Maximum von Mises stress is $\sim 35\text{ MPa}$, which was obtained on a case with the largest x_{bp} . The difference to the case with the smallest x_{bp} is only $\sim 5\text{ MPa}$. Small values of plastic strains are observed ~ 0.0033 .

With this study, we have successfully demonstrated that a combination of RBF-FD method (thermal part) and hybrid RBF-FD method

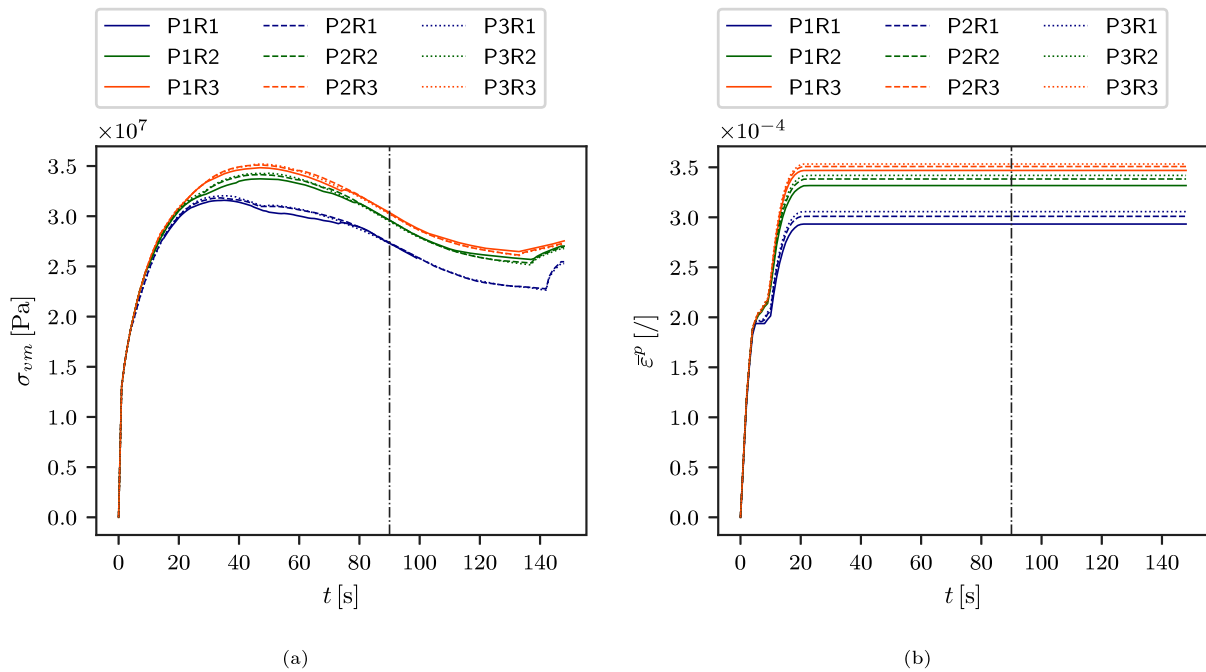


Fig. 17. Maximum values of von Mises stress σ_{vm} (a) and accumulated plastic strain $\bar{\epsilon}^p$ (b) over time.

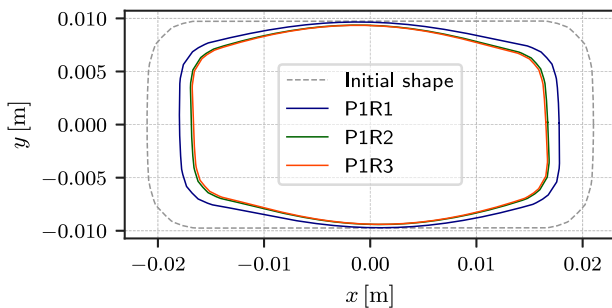


Fig. 18. Contours of initial and final-deformed bars shapes.

(mechanical part) is suitable for analysing the thermo-mechanical response of steel bars on the cooling bed. The proposed method can be applied to optimise the process parameters to obtain the desired temperature, strain, and stress distributions. Also, an input solution field for modelling the straightening process can be generated. The current 2D model can capture only linear axial strains with no self-weight included and no contact with the cooling bed. In future work, we will study bars with different cross-sections that are more prone to bending and residual stress formation. Different orientations of bars and the situations where more than one bar is positioned on the same stage, one on top of the other, which is also being used in the industry, will be investigated. The self-load, expected to impact bending, will be included. The presented model will be next calibrated and validated with the measurements of temperature, deflection, and residual stresses and strains. The present paper demonstrates the industrial use of the meshless method in an area where the finite element method was exclusively dominated.

Declaration of competing interest

The authors have no conflicts of interest to declare that are relevant to the content of this paper.

Data availability

Data will be made available on request.

Acknowledgements

This research was funded by the Slovenian Grant Agency, Slovenia by grant numbers P2-0162, L2-3173, Z2-2640, L2-2609, and Štore-Steel Company (www.store-steel.si). The computations were performed on high-performance computational resources at the Institute of Metals and Technology. The first author was supported by the Young Researcher's grant, Slovenia.

The authors would also like to acknowledge Professor Miroslav Halilovič for the discussions related to the mechanical model and Štefan Obid for the manipulation of the FEM data, both from the Laboratory for Numerical Modelling and Simulation, Faculty of Mechanical Engineering, University of Ljubljana.

References

- [1] Orringer O, Tang YH, Gordon JE, Jeong DY, Morris JM, Perlman AB. Crack propagation life of detail fractures in rails. Final report. Tech. rep. U.S. Department of Transportation; 1988, Number: DOT/FRA/ORD-88/13. URL <https://trid.trb.org/view/287019>.
- [2] Ringsberg JW, Lindbäck T. Rolling contact fatigue analysis of rails including numerical simulations of the rail manufacturing process and repeated wheel-rail contact loads. *Int J Fatigue* 2003;25(6):547–58. [http://dx.doi.org/10.1016/S0142-1123\(02\)00147-0](http://dx.doi.org/10.1016/S0142-1123(02)00147-0), URL <https://www.sciencedirect.com/science/article/pii/S0142112302001470>.
- [3] Nikitin LV, Fischer FD, Oberaigner ER, Rammerstorfer FG, Seitzberger M, Mogilevsky RI. On the frictional behaviour of thermally loaded beams resting on a plane. *Int J Mech Sci* 1996;38(11):1219–29. [http://dx.doi.org/10.1016/0020-7403\(96\)00009-4](http://dx.doi.org/10.1016/0020-7403(96)00009-4), URL <https://www.sciencedirect.com/science/article/pii/0020740396000094>.
- [4] Abouaf M, Chenot J-L, Marcelin J-L. A two-dimensional finite element idealization for thermo-elastic deflection in beams. *Internat J Numer Methods Engrg* 1983;19(10):1453–65. <http://dx.doi.org/10.1002/nme.1620191004>, URL <https://onlinelibrary.wiley.com/doi/abs/10.1002/nme.1620191004>.
- [5] Marcelin JL, Abouaf M, Chenot JL. Analysis of residual stresses in hot-rolled complex beams. *Comput Methods Appl Mech Engrg* 1986;56(1):1–16. [http://dx.doi.org/10.1016/0045-7825\(86\)90133-7](http://dx.doi.org/10.1016/0045-7825(86)90133-7), URL <https://www.sciencedirect.com/science/article/pii/0045782586901337>.

- [6] Boyadjiev II, Thomson PF, Lam YC. Prediction of the deflection and residual stress in controlled cooling of hot-rolled steel beams including load and arbitrary support: Part I. Computational model. *J Mater Process Technol* 2004;147(3):370–6. <http://dx.doi.org/10.1016/j.jmatprotec.2004.01.009>, URL <https://www.sciencedirect.com/science/article/pii/S092401360400041X>.
- [7] Boyadjiev II, Thomson PF, Lam YC. Prediction of the deflection and residual stress in controlled cooling of hot-rolled steel beams including load and arbitrary support: Part II. Experimental validation and application. *J Mater Process Technol* 2004;147(2):268–75. <http://dx.doi.org/10.1016/j.jmatprotec.2004.01.008>, URL <https://www.sciencedirect.com/science/article/pii/S0924013604000408>.
- [8] Basu J, Srimani SL, Gupta DS. Rail behaviour during cooling after hot rolling. *J Strain Anal Eng Des* 2004;39(1):15–24. <http://dx.doi.org/10.1177/030932470403900102>, Publisher: IMECHE.
- [9] Perma Espinoza AV, de Pisón Ascacibar FJM, Limas MC, González Marcos A. Study of cooling strategies for metal profiles through finite element models. IV Jornadas Nacionales Ing Termodinámica 2005. URL https://www.academia.edu/12200538/STUDY_OF_COOLING_STRATEGIES_FOR_METAL_PROFILES_THROUGH_FINITE_ELEMENT_MODELS.
- [10] Smith M. Abaqus/standard user's manual, version 6.9. USA: Dassault Systemes Simulia Corp; 2009.
- [11] Perma-Espinoza A, Ascacibar FJ, Martínez-de Pisón E, Blanco J. Analysis of rail cooling strategies through numerical simulation with instant calculation of thermal expansion coefficient. *Revista Metalurgia* 2010;46. <http://dx.doi.org/10.3989/revmetalm.0911>.
- [12] Tolstykh A, Shirobokov D. On using radial basis functions in a “finite difference mode” with applications to elasticity problems. *Comput Mech* 2003;33(1):68–79. <http://dx.doi.org/10.1007/s00466-003-0501-9>.
- [13] Šarler B, Vertnik R. Meshfree explicit local radial basis function collocation method for diffusion problems. *Comput Math Appl* 2006;51(8):1269–82. <http://dx.doi.org/10.1016/j.camwa.2006.04.013>.
- [14] Mavrič B, Šarler B. Local radial basis function collocation method for linear thermoelasticity in two dimensions. *Internat J Numer Methods Heat Fluid Flow* 2015;25:1488–510. <http://dx.doi.org/10.1108/HFF-11-2014-0359>.
- [15] Flyer N, Fornberg B, Bayona V, Barnett GA. On the role of polynomials in RBF-FD approximations: I. Interpolation and accuracy. *J Comput Phys* 2016;321(1):21–38. <http://dx.doi.org/10.1016/j.jcp.2016.05.026>.
- [16] Xu W-Z, Fu Z-J, Xi Q. A novel localized collocation solver based on a radial Trefftz basis for thermal conduction analysis in FGMs with exponential variations. *Comput Math Appl* 2022;117:24–38. <http://dx.doi.org/10.1016/j.camwa.2022.04.007>, URL <https://www.sciencedirect.com/science/article/pii/S0898122122001560>.
- [17] Fu Z, Tang Z, Xi Q, Liu Q, Gu Y, Wang F. Localized collocation schemes and their applications. *Acta Mech Sin* 2022;38(7):422167. <http://dx.doi.org/10.1007/s10409-022-22167-x>.
- [18] Vuga G, Mavrič B, Šarler B. An improved local radial basis function method for solving small-strain elasto-plasticity. *Comput Methods Appl Mech Engrg* 2024;418:116501. <http://dx.doi.org/10.1016/j.cma.2023.116501>, URL <https://www.sciencedirect.com/science/article/pii/S0045782523006254>.
- [19] Mills AF, Coimbra CFM. Basic heat and mass transfer. 3rd ed. Temporal Publishing, LLC; 2015.
- [20] Howell JR. The Monte Carlo method in radiative heat transfer. *J Heat Transfer* 1998;120(3):547–60. <http://dx.doi.org/10.1115/1.2824310>.
- [21] Jaklič A. Vloga geometrijskega faktorja vidnosti pri optimalnem ogrevanju v kontinuirni peči [Ph.D. thesis], Ljubljana: University of Ljubljana; 2002.
- [22] Jaklič A, Vode F, Kolenko T. Online simulation model of the slab-reheating process in a pusher-type furnace. *Appl Therm Eng* 2007;27:1105–14. <http://dx.doi.org/10.1016/j.applthermaleng.2006.07.033>.
- [23] Hanoglu U, Šarler B. Multi-pass hot-rolling simulation using a meshless method. *Comput Struct* 2018;194:1–14. <http://dx.doi.org/10.1016/j.compstruc.2017.08.012>.
- [24] Hanoglu U, Šarler B. Hot rolling simulation system for steel based on advanced meshless solution. *Metals* 2019;9(7):788. <http://dx.doi.org/10.3390/met9070788>.
- [25] JMatPro. Guildford, UK: Sente Software Ltd., URL <https://www.sentesoftware.co.uk/jmatpro-api>.